

THERMO-MECHANICALLY COUPLED FLUID STRUCTURE INTERACTION FOR THERMAL BUCKLING

K. MARTIN*, AND S. REESE*

*RWTH Aachen University
Institute of Applied Mechanics
Mies-van-der-Rohe-Str. 1, 52070 Aachen, Germany
e-mail: katharina.martin@rwth-aachen.de, e-mail: stefanie.reese@rwth-aachen.de
web page: <http://www.ifam.rwth-aachen.de>

Key words: Finite Elements, Finite strains, Non-linear isotropic and kinematic hardening

Abstract. Experiments have shown that aerothermodynamical loads on thin-walled structures lead under certain constraints to plastic deformation and buckling. The aim of the research is the accurate prediction of thermal buckling behaviour for metallic panels under the before mentioned conditions. In this article the material modelling for thermo-elastoplastic material behaviour is introduced which incorporates non-linear kinematic and isotropic hardening. As a non-linear temperature dependence of mechanical material parameters is included in the model, a special temperature and deformation dependence of the heat capacity is used. This material model is implemented as a user material in *Abaqus* and coupled with the fluid solver *TAU*. As the coupling tool for the fluid-structure interaction *ifls* is used. The results show the expected behaviour and the experimental results of displacement and temperature are reflected in the simulation.

1 INTRODUCTION

Experiments have shown that aerothermodynamical loads induced by high enthalpy flow on thin metallic panels in combination with unavoidable constraints for the movement of the structure might lead to undesirably localized plastic deformation and buckling phenomena. In the considered supersonic flow at Mach numbers of $Ma = 7.62$, the buckling of panels into the stream flow creates shocks and expansion areas which significantly impact the efficiency. In this work the fluid structure interaction between the panel and the flow are shown. The effects of the panel buckling on the flow is shown in Fig. 1. First investigations to thermal buckling were conducted in [12, 1]. The panel buckling is investigated experimentally in a wind tunnel for 120s, where deformation and temperature are measured over time [2]. The panel heats up due to aerothermodynamical loads, pushes against the surrounding frame and buckles into the flow.

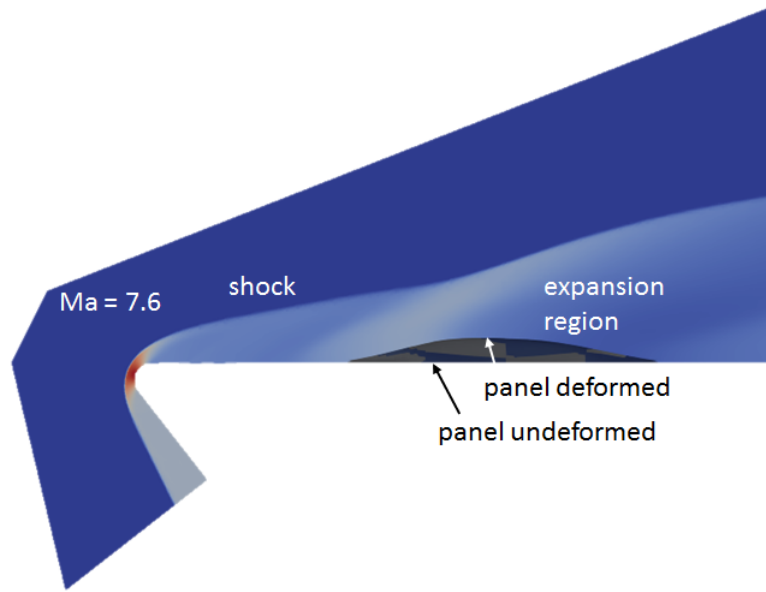


Figure 1: Influence of thermal buckling on fluid flow

An important part of the structural model is the description of the material behaviour. This requires a fully thermomechanical coupled viscoplastic model including large deformations [5]. Therefore a realistic description of the highly temperature- and rate-dependent material behaviour of the structure must be considered. Besides convection and heat radiation, the temperature dependence of the mechanical material behavior as well as the deformation dependence in conduction and capacity terms have to be included in the thermomechanical coupling. For that an extended thermomechanical model is used which takes non-linear thermal evolution into account [9]. This is achieved by defining material parameters which are nonlinearly dependent on the temperature [13, 8]. Therefore, a thermodynamically consistent model of finite thermo-plasticity with non-linear kinematic hardening and isotropic hardening for large deformations is chosen, which is based on [14]. The Helmholtz energy includes nonlinear functions of the temperature and the isothermal energy, which decomposes into an elastic, a kinematic and an isotropic hardening part. This user material is implemented in *Abaqus* as a material subroutine (UMAT). For the fluid simulation a steady state is assumed as the deformation is rather slow: 12 mm in 60 s. The fluid-structure interaction coupling tool *ifls* is provided by the Institute of Aircraft Design and Lightweight Structures (IFL) at TU Braunschweig, which was implemented and extended by [7, 4]. For the fluid computation, *TAU* from the German Aerospace Center (DLR) is used. The fluid-structure interaction focuses on the choice of an equilibrium iteration method, the time integration and the data transfer between grids.

2 Mechanical model

We assume an multiplicative split of the deformation gradient in an elastic and a plastic part $\mathbf{F} = \mathbf{F}_e \mathbf{F}_p$ and another split of the plastic part in an elastic and inelastic, motivated by the findings of [6]. The right Cauchy-Green tensor is given by $\mathbf{C} = \mathbf{F}^T \mathbf{F}$, the elastic part $\mathbf{C}_e = \mathbf{F}_e^T \mathbf{F}_e$ and the elastic plastic part \mathbf{C}_{pe} of the right Cauchy-Green tensor respectively. The following Helmholtz free energy is proposed, which includes thermal expansion and temperature dependence of the material parameters [9]:

$$\Psi = \frac{\Theta}{\Theta_0} \Psi_0 - \Lambda(\Theta) \alpha(\Theta) (\theta - \theta_0) (J - 1) \quad (1)$$

Whereas $\Lambda(\Theta)$ is the temperature dependent Lamé constant, $\alpha(\Theta)$ the temperature dependent thermal expansion coefficient, θ the temperature, θ_0 is the reference temperature, J is given as $\det \mathbf{F}$ and Ψ_0 is additively split into an elastic part, an isotropic hardening part and an kinematic hardening part. For the elastic part a standard Neo-Hooke form is chosen. The isotropic part is a von-Voigt-type function and the kinematic part is chosen according to [14, 3]:

$$\Psi_e = -\frac{\mu(\Theta)}{2} (\text{tr} \mathbf{C}_e - 3) - \mu(\Theta) \ln \left(\sqrt{\det \mathbf{C}_e} \right) + \frac{\Lambda(\Theta)}{4} (\det \mathbf{C}_e - 1 - 2 \ln(\det \mathbf{C}_e)) \quad (2)$$

$$\Psi_{iso} = -H(\Theta) \left(\kappa + \frac{e^{-\beta(\Theta)\kappa} - 1}{\beta(\Theta)} \right) \quad (3)$$

$$\Psi_{kin} = -\frac{c(\Theta)}{2} (\text{tr} \mathbf{C}_{pe} - 3) - c(\Theta) \ln \left(\sqrt{\det \mathbf{C}_{pe}} \right) \quad (4)$$

Whereas $\mu(\Theta)$ is the shear modulus, κ is the isotropic hardening variable, $H(\Theta)$ and $\beta(\Theta)$ are material parameters for the isotropic hardening part, $c(\Theta)$ and $b(\Theta)$ material parameters for the nonlinear kinematic hardening part. All material parameters are temperature dependent. To fulfill the second law of thermodynamics the proposed Helmholtz free energy is inserted into the Clausius-Duhem-inequality

$$-\dot{\Psi} + \mathbf{S} \cdot \frac{1}{2} \dot{\mathbf{C}} > 0 \quad (5)$$

whereas \mathbf{S} is the second Piola-Kirchhoff stress tensor. It yields

$$\left(\mathbf{S} - 2\mathbf{F}_p^{-1} \frac{\partial \Psi}{\partial \mathbf{C}_e} \mathbf{F}_p^{-T} \right) \cdot \frac{1}{2} \dot{\mathbf{C}} + (\mathbf{M} - \boldsymbol{\chi}) \cdot \mathbf{d}_p + \mathbf{M}_{kin} \mathbf{d}_{p_i} - \frac{\partial \Psi}{\partial \kappa} \dot{\kappa} > 0 \quad (6)$$

For arbitrary $\dot{\mathbf{C}}$, \mathbf{d}_p , \mathbf{d}_{p_i} and $\dot{\kappa}$, the second Piola Kirchhoff stress tensor is

$$\mathbf{S} = 2\mathbf{F}_p^{-1} \frac{\partial \Psi}{\partial \mathbf{C}_e} \mathbf{F}_p^{-T} \quad (7)$$

The remaining dissipation inequality yields

$$(\mathbf{M} - \boldsymbol{\chi}) \cdot \mathbf{d}_p + \mathbf{M}_{kin} \mathbf{d}_{p_i} - \frac{\partial \Psi}{\partial \kappa} \dot{\kappa} > 0 \quad (8)$$

whereas the two symmetric Mandel stress tensors

$$\mathbf{M} = 2\mathbf{C}_e \frac{\partial \Psi}{\partial \mathbf{C}_e}, \quad \mathbf{M}_{kin} = 2\mathbf{C}_{pe} \frac{\partial \Psi}{\partial \mathbf{C}_{pe}} \quad (9)$$

and the back stress and drag stress tensor is given by

$$\boldsymbol{\chi} = 2\mathbf{F}_{pe} \frac{\partial \Psi}{\partial \mathbf{C}_{pe}} \mathbf{F}_{pe}, \quad R = -\frac{\partial \Psi}{\partial \kappa} \quad (10)$$

The evolution equation are chosen that they fulfill the dissipation inequality

$$\mathbf{d}_p = \dot{\lambda} \frac{\partial \Psi}{\partial \mathbf{M}}, \quad \mathbf{d}_{p_i} = \dot{\lambda} \frac{b(\Theta)}{c(\Theta)} \mathbf{M}_{kin}^D, \quad \kappa = \sqrt{\frac{2}{3}} \dot{\lambda} \quad (11)$$

A von-Mises yield function is chosen:

$$\Phi = \|\mathbf{M}^D - \boldsymbol{\chi}^D\| - \sqrt{\frac{2}{3}}(\sigma_y(\Theta) - R) \quad (12)$$

with the drag stress derived to $R = -H(\Theta)(1 - e^{-\beta(\Theta)\kappa})$. As the equations are all in different configurations, they are transfered to reference configuration as due to the symmetric quantities the system of equations reduces to 14.

3 Fluid calculation

The freestream conditions, which have been also used for the experiments [2] are given table 3. The fluid calculation is preformed with the program *TAU* from the German

Ma_∞	7.62
T_∞	463.7 K
p_∞	52 Pa
Pr	0.72
γ	1.462
R	346 J/(kg K)

Table 1: Freestream conditions [2]

Aerospace Center (DLR). For the fluid simulation a Reynolds-Average-Navier-Stokes (RANS) is used. For the spatial discretization is the AUSMDV-Upwind method used and for the time intergration a pseudo 3rd-order Runge-Kutta method. In Fig. 2 the fluid grid is shown with refinement at the shock interface of the detached bow shock and the boundary layer. The region at the isentropic compression at the beginning of the deformed panel is not yet refined. A more detailed investigations is needed.

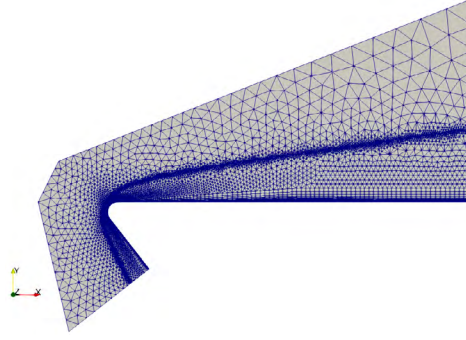


Figure 2: Fluid mesh with refinement at shock interface and boundary layer

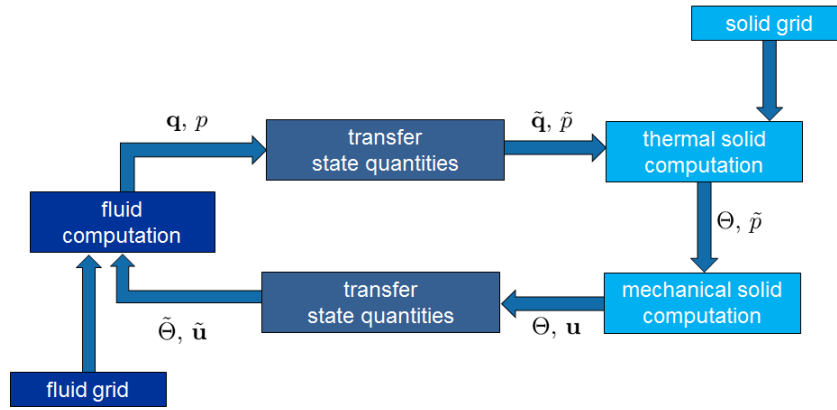


Figure 3: Coupling scheme of *ifls*

4 Fluid-structure interaction

For the fluid-structure interaction the code *ifls* from the Institute of Aircraft Design and Lightweight Structures (IFL) at TU Braunschweig is used. It provides a coupling domain for several structural and fluid solvers, e.g. *Abaqus FEA* and *TAU*. As the structural deformation is rather slow an equilibrium state for fluid and solid can be assumed in each time step. For the equilibrium iteration method the Dirichlet-Neumann method is used. The Dirichlet problem is solved in the fluid calculation, where the temperature $\tilde{\Theta}$ and the displacement $\tilde{\mathbf{u}}$ is held fixed at the domain surfaces. The Neumann problem is solved in the structural computation, where the heat flux \mathbf{q} and the pressure p are applied to the domain surfaces. For the transfer of the state quantities a Lagrange multiplier is used for non-conforming meshes. For the time intergration an iterative staggered procedure is used. The coupling scheme is schematically shown in Fig. 3. The ternal and mechanical computation of the structural is not yet fully coupled. The heat flux and pressure are applied to a thermal computation in a first step, in which temperature boundary conditions for a mechanical structural computation are calculated. This is used to calculate the thermal

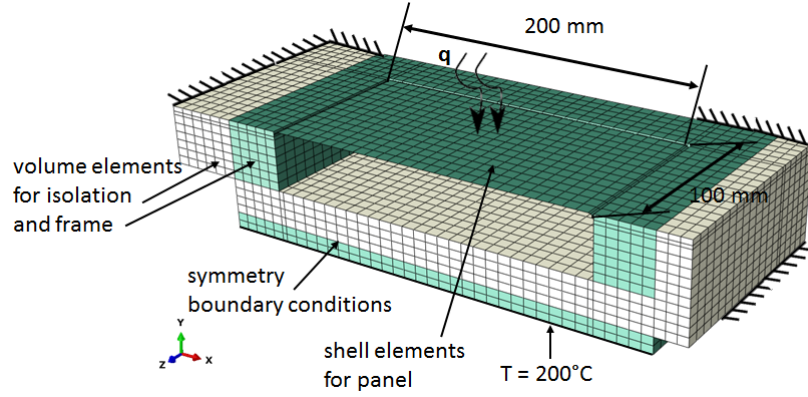


Figure 4: Boundary conditions for structural model

Position	x [mm]	z [mm]
front	50	0
center	100	0
back	150	0

Table 2: Measurement positions [2]

expansion in the second structural computation. The state quantities $\tilde{\mathbf{q}}$, \tilde{p} , $\tilde{\Theta}$, $\tilde{\mathbf{u}}$ refer to the fluid mesh. The values \mathbf{q} , p , Θ , \mathbf{u} refer to the solid grid, respectively.

5 Structural model

For the thermal solid computation a standard *Abaqus* heat transfer and radiation model was used. For the mechanical solid computation the above introduced material model was incorporated as a user material routine (UMAT) in *Abaqus* for shell elements. The mechanical model is shown in 4. The clamped support for the structural part are indicated only at the edges but apply to all nodes except the panel. The thermal boundary conditions are as follows: the bottom is fixed at $T = 200^\circ\text{C}$ and from the top the heat flux is given from the fluid computation. For the panel shell elements (S4) are used. For the frame (green) and isolation (white) volume elements (C3D8) are used. The material of the panel and frame is Incoloy 800HT and for the isolation Schupp Ultra Board 1850/500 by Schupp Industriekeramik is used. Material parameters are taken from [11, 2]. The panel is discretized by 234 elements and five integration points are used over the thickness. The bending radius is discretized by 4 elements in circumference direction.

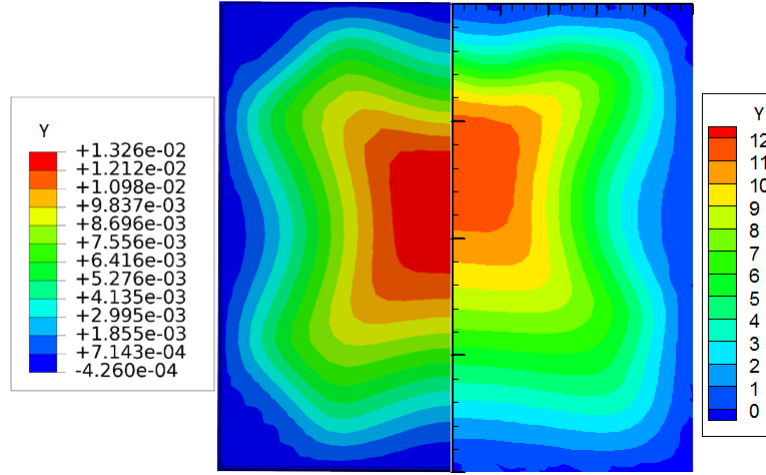


Figure 5: Displacement contour plot at $t = 60$ s; left: Simulation [m], right: experiment [mm]

6 Results

6.1 Solid

For the displacement and temperature results the same coordinate positions for the measurement are used. The coordinates are given in Tab. 6.1 and lay on the centerline of the panel in flow direction. The comparison between the experimental and simulation results of the displacement are shown in 6. The maximum displacement in z-direction is 13.26 mm for the simulation and 11.8 mm for the experiment. This correlates to an error of 12.4%. The buckling form is similar. The maximum buckling position of the simulation is positioned more to the center of the panel. This correlates to the results of the temperature distribution. The point of the maximum temperature in the simulation is positioned more to the middle. This is shown in Fig. 6, where the temperature in the front is underestimated and overestimated in the middle. In the structural calculation the rounded nose, which can be seen in the fluid model is not modeled. As an isolation is located between the rounded nose and the frame, it should not have a big influence on the temperature distribution and displacement of the model but will be investigated in future works.

6.2 Fluid

The results from the fluid calculation are shown for the Mach number in Fig. 7 and for the c_p -distribution in Fig. 8 for the times $t = 0$ s, $t = 30$ s, $t = 60$ s and $t = 120$ s. At $t = 0$ s the panel has not yet started to buckle into the stream, therefore the undisturbed flow field is shown. A detached bow shock is located at the round nose. At $t = 30$ s the panel had began to buckle into the flow and an isentropic compression region is formed at the beginning of the panel as the deformation is not convex. This leads to an expansion of the nose shock when the isentropic compression interacts with the bow shock. From

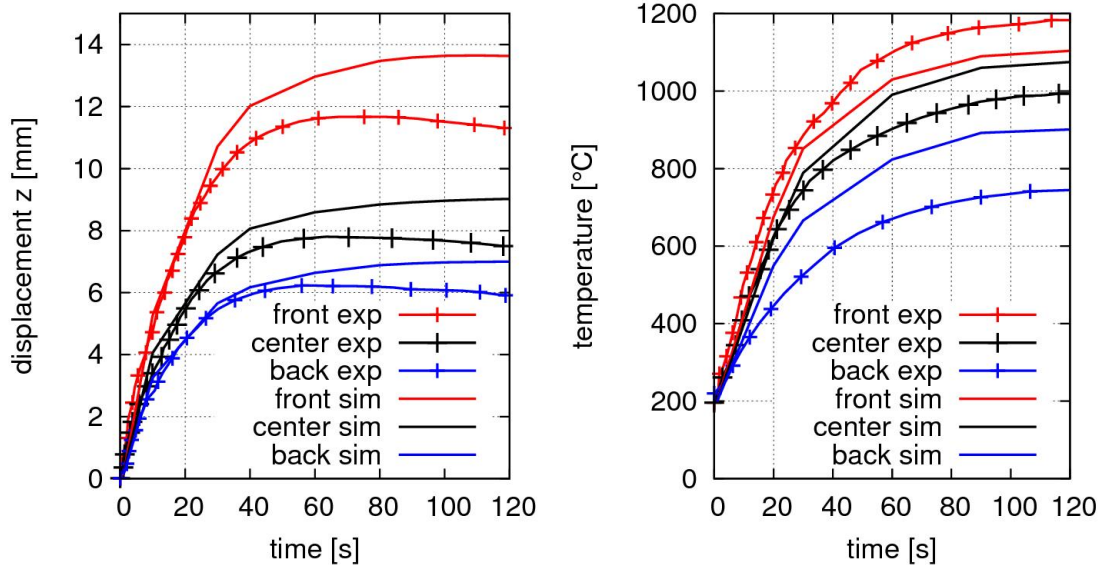


Figure 6: Displacement over time (left), temperature over time (right) - comparison between simulation and experiment

the highest buckling point a Prandtl-Meyer expansion begins, where the fluid accelerates and pressure decreases. At $t = 60$ s, the shock expands more until $t = 120$ s, where the maximum amplitude is reached.

7 Conclusion

A thermo-elastoplastic material model with non-linear isotropic and kinematic hardening for finite strains and with temperature dependent material parameters was introduced. This material model was implemented as a material user subroutine in *Abaqus* and coupled with the fluid solver *TAU*. The coupling domain was provided by *ifls* which is a coupling tool for thermal-mechanical fluid-structure interaction. The comparison of temperature and displacement between simulation and experiment shows good agreement. The boundary conditions from the experiments must be incorporated in more detail for fluid and solid, e.g. a three-dimensional flow around the panel and chemical non-equilibrium for the fluid and adapted mechanical and thermal boundary conditions for the structural computation.

8 Acknowledgements

Financial support has been provided by the DFG in the framework of Transregio 40 'Fundamental Technologies for the Development of Future Space-Transport-System Components under High Thermal and Mechanical Loads' (TP D10). Further, the financial support of the project 'Towards a model based control of biohybrid implant maturation (DFG PAK 961 P3)' is gratefully acknowledged.

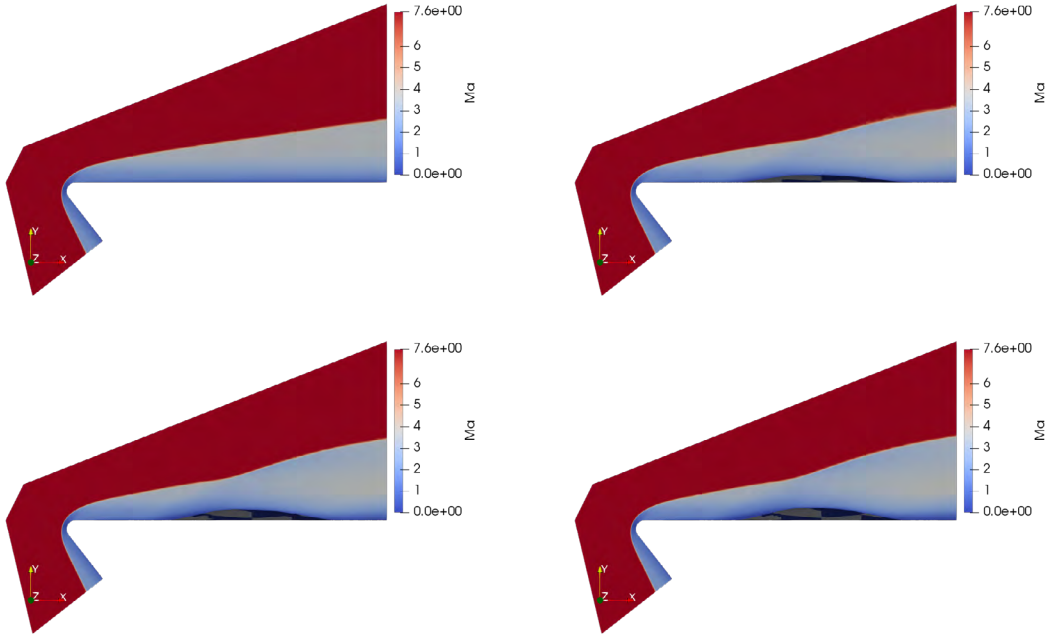


Figure 7: Mach number at $t = 0$ s (top left), $t = 30$ s (top right), $t = 60$ s (bottom left) and $t = 120$ s (bottom right); max=7.6

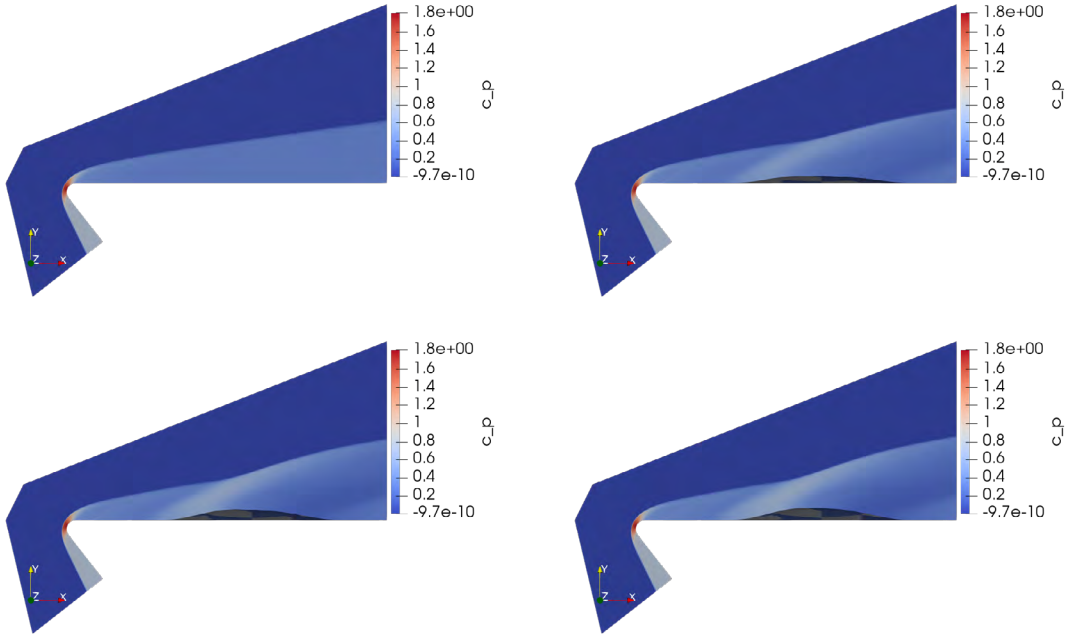


Figure 8: c_p distribution at $t = 0$ s (top left), $t = 30$ s (top right), $t = 60$ s (bottom left) and $t = 120$ s (bottom right); max=1.8

REFERENCES

- [1] Culler, A. and McNamara, J.J. *Impact of Fluid-Thermal-Structural Coupling on Response Prediction of Hypersonic Skin Panels*. The American Institute of Aeronautics and Astronautics Journal; Vol. 49:2393-2406, (2011).
- [2] Daub, D., Esser, B., Willems, S. and Gülhan, A. Experimental Studies on Aerothermal FSI with Plastic Deformation. *SFB/TRR40 Annual Report* (2018).
- [3] Dettmer, W. and Reese, S. On the theoretical and numerical modelling of Armstrong-Frederick kinematic hardening in the finite strain regime. *Computer methods in applied mechanics and engineering*; Vol. 193:87-116, (2003).
- [4] Haupt, M., Niesner, R., Unger, R. and Horst, R. Model configuration for the validation of aerothermodynamic thermal-mechanical fluid-structure interactions. *ASME 2012, 11th Biennial Conference On Engineering Systems Design and Analysis* (2012).
- [5] Hollstein, T. and Voss, B. Experimental Determination of the High-Temperature Crack Growth Behavior of Incoloy 800H. *Nonlinear Fracture Mechanics: Volume I - Time-Dependent Fracture, ASTM STP 99*; Vol. 1:195-213, (1989).
- [6] Lion, A. Constitutive modelling in finite thermoviscoplasticity: a physical approach based on nonlinear rheological models. *International Journal of Plasticity*; Vol. 16:469-494, (2000).
- [7] Niesner, R. *Gekoppelte Simulation thermisch-mechanischer Fluid-Struktur-Interaktion für Hyperschall-Anwendungen*. PhD Thesis; Technische Universität Carolo-Wilhelmina zu Braunschweig (2008).
- [8] Nowinski, J.L. *Theory of thermoelasticity with applications*, Spring Netherlands, (1978).
- [9] Reese, S. and Govindjee, S. Theoretical and Numerical Aspects in the Thermo-Viscoelastic Material Behaviour of Rubber-Like Polymers. *Mechanics of Time-Dependent Materials*; Vol. 1:357-396, (1998).
- [10] Reese, S. and Wriggers, P. A material model for rubber-like polymers exhibiting plastic deformation: computational aspects and a comparison with experimental results. *Computer methods in applied mechanics and engineering*; Vol. 148:279-298, (1997).
- [11] Special Metals Wiggin Limited *Incoloy alloy 800H and 800HT*. www.specialmetals.com; (2004).
- [12] Thornton, E.A. and Dechaumphai, P. Coupled Flow, Thermal, and Structural Analysis of Aerodynamically Heated Panels. *Journal of Aircraft*; Vol. 25:1052-1059 (1988).

- [13] Treloar, L.R.G. *The Physics of Rubber Elasticity*. Oxford University Press, USA, (1975).
- [14] Vladimirov, I. N., Pietryga, M. P., Reese, S. On the modelling of non-linear kinematic hardening at finite strains with application to springback - Comparison of time integration algorithms. *Int. J. Numer. Meth. Engng*; Vol. 75:1-28, (2007).